Article

Effect of Hydrogen Charging on the Stress Corrosion Cracking Behavior of X70 Steel in Simulated Deep Seawater Environment

Xiaojia Yang [1,2,*] , Feilong Sun [3], Qing Li [2], Renzheng Zhu [2], Zhiyong Liu [2,*], Cuiwei Du [2] and Xiaogang Li [2]

[1] Shunde Graduate School, University of Science and Technology Beijing, Foshan 528399, China
[2] National Materials Corrosion and Protection Data Center, University of Science and Technology Beijing, Beijing 100083, China; lq@tydnm.com (Q.L.); d202110654@ustb.xs.edu (R.Z.); dcw@ustb.edu.cn (C.D.); lixiaogang@ustb.edu.cn (X.L.)
[3] China Building Material Test & Certification Group Co., Ltd., Beijing 100024, China; seney612@163.com
* Correspondence: yangxiaojia@ustb.edu.cn (X.Y.); liuzhiyong7804@126.com (Z.L.)

Abstract: The effects of hydrogen charging on the electrochemical and stress corrosion cracking (SCC) behavior of X70 steel in a simulated deep seawater environment were investigated by using electrochemical measurements, slow strain rate tensile (SSRT) tests, and corrosion morphology characterization through SEM. The results showed that the concentrations of the adsorbed hydrogen in X70 steel after precharging under different hydrostatic pressures increased gradually and tended to be steady with the charging time. High hydrostatic pressures promoted the hydrogen permeation of X70 pipeline steel by promoting the permeating rate and quantity. The SCC susceptibility of X70 steel decreased first and then increased with the hydrogen-charging current density. The area reduction loss (I_ψ) and true strain loss (I_ε) exhibited the lowest SCC susceptibility at the 25 mA/cm^2 hydrogen-precharging current density. The elongation rate loss (I_δ) exhibited the lowest SCC susceptibility at the 50 mA/cm^2 hydrogen-precharging current density.

Keywords: X70; hydrogen penetration; deep seawater; SCC

1. Introduction

Oil and gas will continue to be the dominant source of energy resources across the world in the future. Due to the rapid exploration and development of offshore oil and gas, oil and gas resources in deep sea have been considered the major production sources in the exploitation field, and they have led to a large scale of pipeline steels in service. Due to the aggressive marine environment and the complexity of oil and gas production, there may be a high risk of failure for subsea pipelines caused by the combined factors of corrosion, stress corrosion cracking (SCC), hydrostatic pressure, waves, and currents, as well as some emergency events. As a result, huge economic losses and serious environmental pollution occur.

SCC is one of the main failure modes because of the offshore pipeline usually laid directly on the seabed or suspended to the offshore platform. Therefore, changes in a number of aspects including seabed topography, ocean currents, and geological factors produce additional structural tensile stresses. Moreover, high-level tensile stress within local pipeline segment, due to various superpositions of structural stress/strain, hoop stress, and residual stress in weld joints, may exceed the critical level in the occurrence of SCC [1]. Meanwhile, the disbanding and peeling of coatings lead to the direct contact of corrosive media on the surface of pipeline steels. Under these synergetic effects, it can be strongly confirmed that it is highly risky of SCC failure for subsea pipelines.

Although quite a few SCC accidents have been recognized in deep-sea environments, a number of accidents caused by the SCC of oil/gas pipelines in land soil have been characterized in recent years [2–7], which are mainly divided into high-pH SCC and near-neutral-pH SCC [8–11]. High-pH SCC often occurs in places where cathodic protection (CP)

is strong with localized pH values higher than nine, while near-neutral-pH SCC usually takes place in weak-CP or no-CP areas [12,13]. The above situations can be more severe, as the service condition is much more complex in subsea environments. Moreover, the penetration of seawater into the gaps will promote the peeling of coatings, creating a more complex corrosion environment. Therefore, it is believed that high-pH or near-neutral-pH environments with a higher concentration of chloride ions can form under peeled coatings, and SCC is easily initiated in such situations [14,15].

Many studies have categorized the mechanisms of SCC into three ways, i.e., anodic dissolution (AD), hydrogen embrittlement (HE), and their mixed influences [16,17]. Like terrestrial pipelines, subsea pipelines were also installed with CP. Therefore, once the coating is destroyed or cathodically disbanded by over-CP, seawater will permeate into the gaps and lead to corrosion [18]. The SCC caused by HE is a severe environmental type of failure that affects almost all metals and alloys [19]. Studies indicated that the cathodic reaction of X70 steel in deep-seawater environments is hydrogen evolution [20,21]. The precipiation of hydrogen may be due to corrosion in aqueous media (including pickling), excessive CP, electroplating (without baking), welding by using damp electrodes, hydrogen gas (if moist) used as a coolant in generators, etc. Hydrogen can initially be present, either externally or internally, within the bulk of a structural alloy. The introduced hydrogen atoms can be adsorbed on the electrode surface and diffused to the internal metal matrix. As a result, the slip resistance of the dislocation decreases, and the dislocation density increases simultaneously. When the hydrogen concentration reaches the threshold value, the main dislocations are amalgamated at the aggregation source, resulting in a local shear stress and promoting the initiation of cracks. Therefore, the cathodic hydrogen evolution plays a significant role in the SCC susceptibility of X70 steel in the simulated seawater environment. Although HE has been extensively studied by many researchers, neither a clear interpretation nor a unified recognition of the mechanics has been achieved yet.

In recent years, the most recognized mechanisms of HE mainly includes stress-induced hydride formation and cleavage [22], hydrogen-enhanced localization plasticity (HELP) model [23], and hydrogen-enhanced decohesion (HEDE) [24,25]. Generally, the HELP model is more suitable for plastic fracture, and HEDE is more suitable for brittle fracture. Although various mechanisms have been proposed, an accurate understanding of the effect of hydrogen on the SCC behavior of X70 pipelines is still insufficient. Electrochemical methods based on the oxidation of reduced hydrogen absorbed in metals and the slow strain rate test method are still powerful tools for studying the effect of hydrogen on the SCC behavior of metals.

In this paper, the effect of hydrogen on the SCC process was investigated with the electrochemical hydrogen permeation method. A great deal of attention has been paid to the effect of the hydrogen current density on the SCC behavior under high hydrostatic pressure. The critical hydrogen concentration of the SCC susceptibility transition point of X70 pipeline steel was confirmed by calculating the average hydrogen density on the surface at various hydrogen-charging current densities.

2. Materials and Methods

2.1. Material and Samples

Slow strain rate tensile (SSRT) test specimens were manufactured with a rolled X70 steel sheet. The X70 steel was provided by Nanjing Iron & Steel United Co., Ltd., Nanjing, Jiangsu, China. The schematic diagram is represented in Figure 1. The chemical compositions were 0.045 wt% C, 1.53 wt% Mn, 0.013 wt% P, 0.0036 wt% S, 0.20 wt% Si, 0.048 wt% V, 0.030% wt% Cr, 0.0031 wt% Cu, 0.020 wt% Ni, 0.15 wt% Mo, and Fe-balanced. After polishing and cleaning, a dehydrogenation procedure was performed, by annealing the X70 specimens at 200 °C for 2 h and slowly cooling them to room temperature in an automatic furnace with a nitrogen inert environment. Prior to each test, the SCC specimens were ground in a longitudinal direction by a successive emery paper up to 2000 grit and then embedded in an epoxy resin with a working area of 0.75 cm^2. Then, the specimens

were rinsed with deionized water, degreased in dehydrated ethanol and acetone with ultrasonic cleaning apparatus and subsequently dried in air.
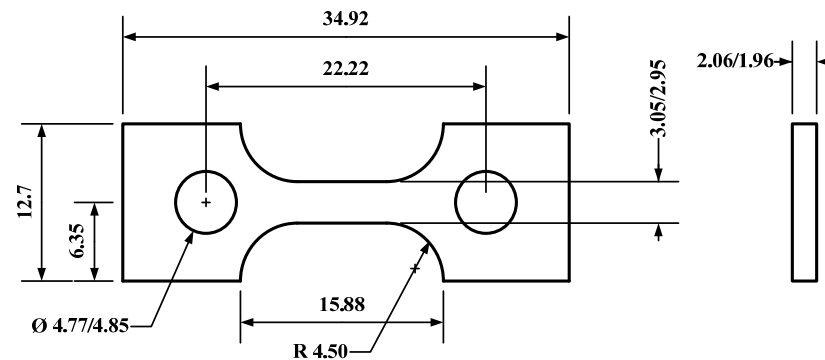
NOTE: ALL DIMENSIONS SHOWN IN MILLIMETERS

Figure 1. Schematic diagram of slow strain rate tests specimens.

2.2. Cathodic Hydrogen Charging

Cathodic hydrogen-charging specimens were prepared in duplicate for hydrogen concentration measurements and SSRT tests. Hydrogen charging tests were carried out in a 0.2 mol/L NaOH solution and poisoned with 0.25 g/L thiourea as a hydrogen recombination inhibitor at room temperature. The hydrostatic pressures for hydrogen charging were 0.1 and 5 MPa, which were pressurized by high-purity nitrogen. Before each experiment, the electrolyte was de-oxygenated by pure nitrogen bubbling for 1 h. The charging current densities employed were in the range of 10–1000 mA/cm^2, while the charging time varied from 2 to 24 h.

2.3. Hydrogen Concentration Measurement

After hydrogen charging was finished, some specimens were cleaned with a 0.2 mol/L NaOH solution once and then quickly transferred to a 0.2 mol/L NaOH solution to test the hydrogen concentration. Before each experiment, the electrolyte was deoxygenated by pure nitrogen bubbling for 1 h and kept until the test process was terminated (throughout the whole test process). The tests were carried out using a three-electrode electrochemical cell with a saturated calomel electrode (SCE) as the reference electrode and a platinum sheet as the auxiliary electrode. An additional potential of +168 mV was applied to the work electrode to monitor the anodic current variation. To obtain the hydroxide current, this anodic current should be corrected by subtracting the background current, which was obtained from the blank experiments with uncharged specimens.

2.4. SSRT Test

The SSRT method was used to investigate the SCC behavior of X70 steel after cathodic hydrogen charging in a simulated 500 m deep seawater environment. SSRT tests were conducted on an electrochemical slow strain rate machine (LF-100-201-V-304, Thermo Electron Corporation, Waltham, MA, USA), with a strain rate of 1.2×10^{-6} s^{-1}. The control loop of the slow strain rate machine was crosshead displacement-driven by a servo motor. The solution used in the tests was artificial seawater with pH of approximately 8.0 and pressurized by high-purity nitrogen to about 5 MPa. The test temperature was set at the ambient environment (approximately 25 °C). All the tensile tests were performed without the use of an extensometer. In order to calculate the strain, the gauge lengths of the specimens were marked and measured before and after fracture. During the test, the stress–strain curve was recorded to compare the ductile loss of the specimens. After failure, the percentage of elongation and the area reduction of each specimen were calculated after removing corrosion products. In addition, the fracture morphologies were observed using a scanning electron microscope. Each test was reproduced at least three times to ensure

the reliability of experimental data. Afterwards, the cross-sectional morphologies of the fracture were observed to investigate the fracture location and cracking mode.

2.5. Hydrogen Analysis

The content of hydrogen in the metal matrix can be determined by the electrochemical oxidation method. When the charged sample is in an anodic electric field and in a NaOH solution, the hydrogen atoms in a subsurface diffuse from the metal matrix to the electrode surface. It can be oxidized to H^+ to form a hydroxide current density (i_H) on the electrode surface shown in Equation (1):

$$H \rightarrow H^+ + e^-. \tag{1}$$

The i_H has a proportional relationship with the hydrogen atoms density on the metal surface. The hydrogen damage susceptibility can be evaluated by the adsorbed hydrogen concentration (C) as calculated with i_H and the quantity of electric charge (Q), where Q can be acquired from the integration value of the i_H–t curve. The relationship of C with Q is shown in Equation (2), which is an established method, and it was firstly introduced by Yan et al. [26]:

$$C = \frac{Q}{zFv}, \tag{2}$$

where F is the Faraday constant, v is the effective volume of the specimen, and z is the electronic number.

Investigations indicate that there is a square root relationship between the adsorbed hydrogen concentration and the hydrogen-charging current density, shown as following:

$$C \propto i_c^{1/2}. \tag{3}$$

Cathodic hydrogen charging is widely used as an efficient way for the hydrogen charging of metallic materials. The hydrogen retention ratio represents the relationship between the inner hydrogen diffusion rate and the outer hydrogen-biding rate, and it is shown in Equation (4):

$$R = \frac{Q}{i_c t_0}, \tag{4}$$

where R is the hydrogen retention ratio and t_0 is the hydrogen-precharging time. From Equations (2)–(4), we can get the square root relationship [26] between R and i_c, as shown in Equation (5):

$$R \propto i_c^{-1/2}. \tag{5}$$

An anodic potential of +168 mV was applied to the blank specimen to test the background current i_0. The hydroxide current i_H was obtained from the anodic current at +168 mV by removing the effect of the background current, as illustrated in Figure 2.
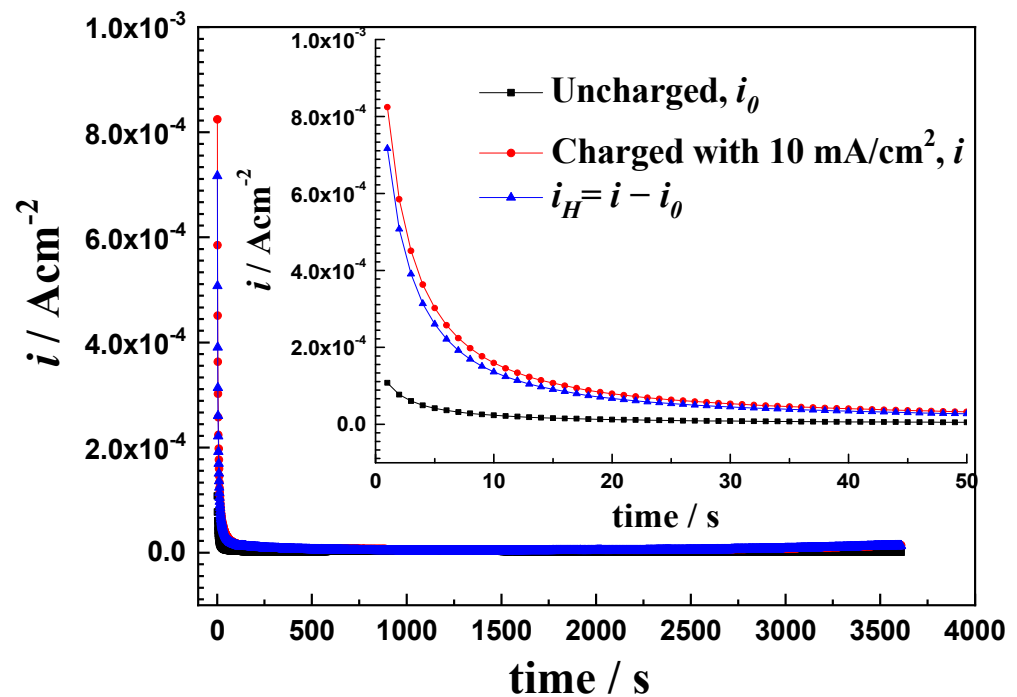
Figure 2. Method interpretation of calculating the hydroxide current after a 2 h hydrogen precharging of X70 steel under a 0.1 MPa hydrostatic pressure.

3. Results

3.1. Effect of the Hydrostatic Pressure on the Hydrogen Permeation Behavior of X70 Steel

Figures 3 and 4 depict the variation of the hydroxide current i_H of the X70 specimens with the time at the condition of different cathodic hydrogen-charging times at 0.1 and 5 MPa hydrostatic pressures. From the results, we can see that the hydroxide current i_H increased with the charging time under different hydrostatic pressures. The electric quantity Q can be obtained by integrating every single i_H–t curve, and the adsorbed hydrogen concentration C can be calculated from Equation (2). Figure 5 shows the variation of the adsorbed hydrogen concentration with the time under 0.1 and 5 MPa hydrostatic pressures. With the extension of the hydrogen-charging time, the concentration of the adsorbed hydrogen increased gradually and tended to be stable. Comparing the hydrogen permeation kinetics curves under different hydrostatic pressures, we can see that both the hydrogen permeation speed and the quantity were promoted by the hydrostatic pressure.

3.2. Effect of the Hydrogen-Charging Current Density on the Hydrogen Permeation of X70 Steel under High Hydrostatic Pressure

Based on the analysis above, the hydrostatic pressure promoted the hydrogen permeation rate and the permeation quantity of X70 steel under a constant hydrogen-charging current density. In this study, the effect of the cathodic hydrogen-charging current density on the hydrogen permeation behavior was also studied. Figure 6 depicts the variation of i_H with the time under various current densities of 10, 25, 50, 100, 200, and 1000 mA/cm^2 for 24 h.

Figure 7 shows the variation of the adsorbed hydrogen concentration C with the charging current density of X70 steel. It depicts that the average hydrogen concentration increased with the charging current density, and a linear relationship can be found with the square root value of the charging current density. It was in association with Equation (6):

$$C = (1.730 \pm 0.223) + (1.047 \pm 0.223) \times i_c^{1/2}. \tag{6}$$
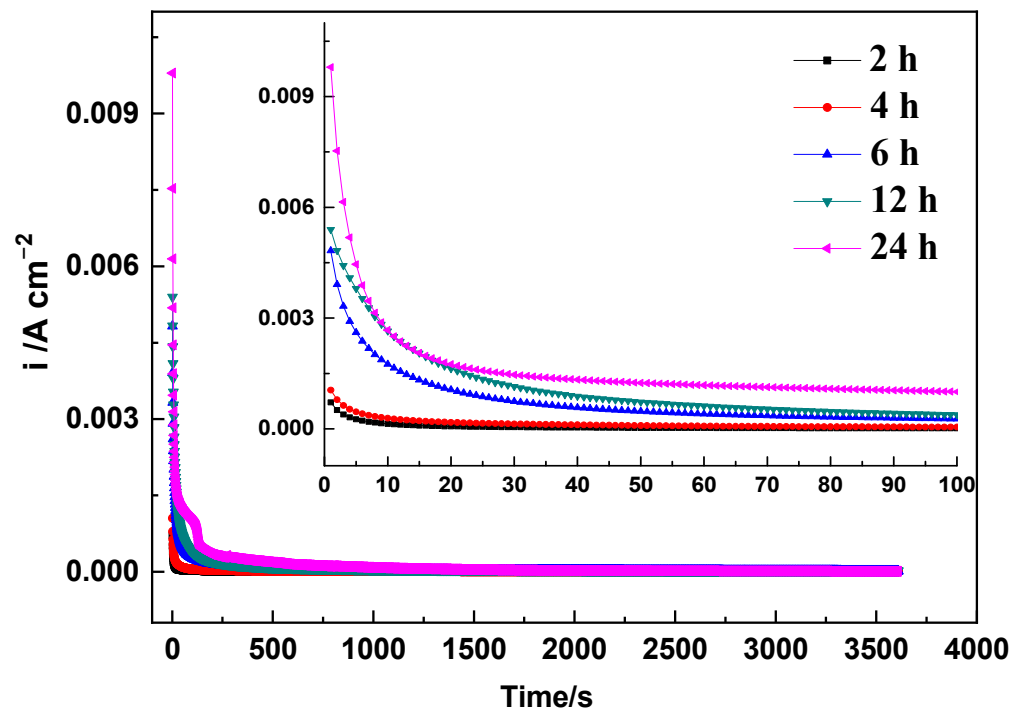
Figure 3. Comparison of the hydroxide currents with different hydrogen-charging times of X70 steel under the 0.1 MPa hydrostatic pressure.
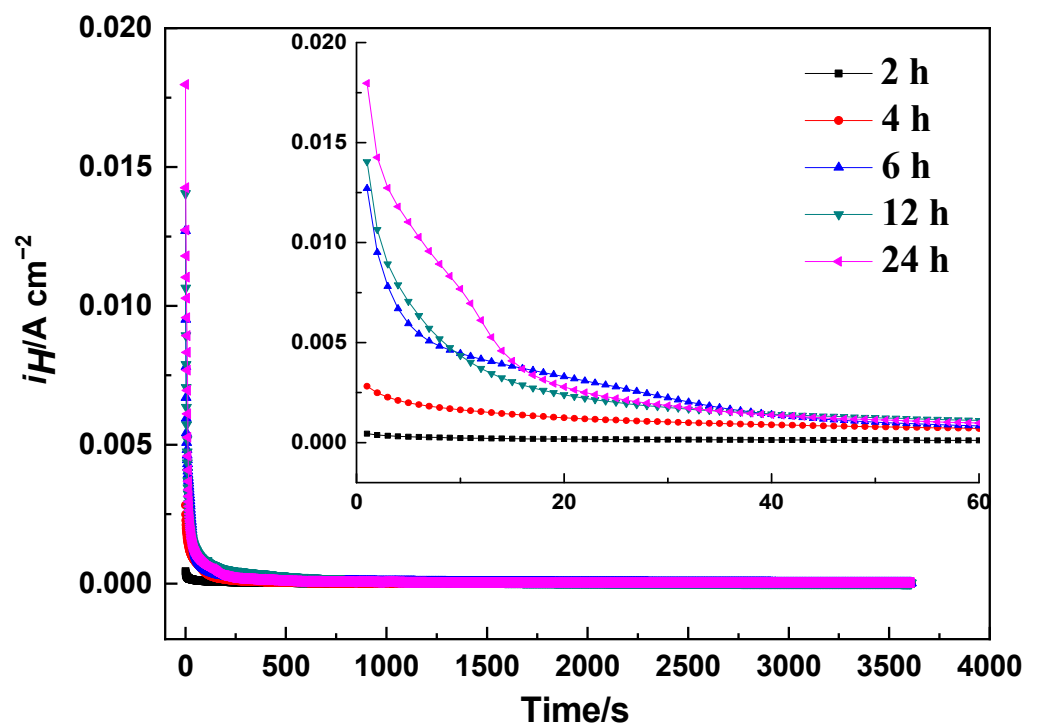
Figure 4. Comparison of the hydroxide currents with different hydrogen-charging times of X70 steel under the 5 MPa hydrostatic pressure.
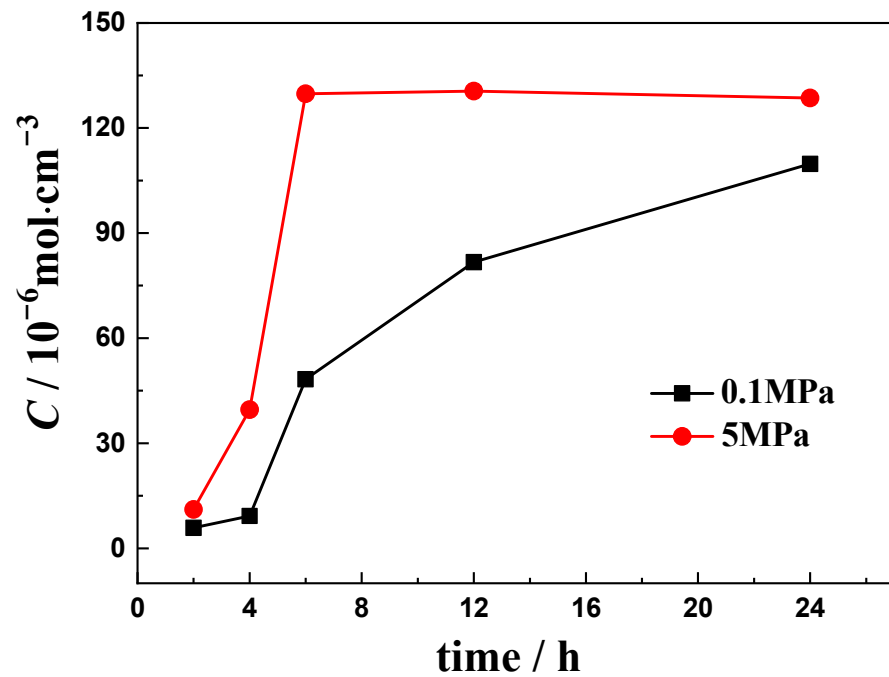
Figure 5. Comparison of the hydrogen concentrations with different hydrogen-charging times of X70 steel under 0.1 and 5 MPa hydrostatic pressures.
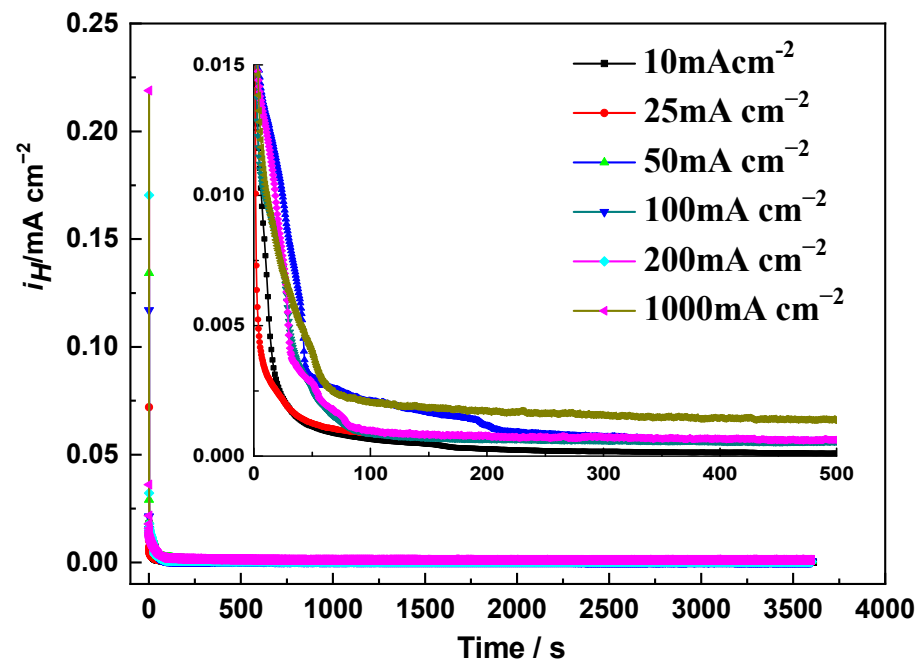
Figure 6. Variation of i_H with the time under various current densities of 10, 25, 50, 100, 200, and 1000 mA/cm² for 24 h.

The hydrogen retention rate (*R*) can be calculated through Equation (4). Figure 8 represents the variation of *R* with the charging current density. It depicts that the *R* decreased as the i_c increased. Besides, a linear relationship with the reciprocal square root value of the charging current density can be detected, and it was associated with Equation (7):

$$R = (-2.533 \pm 0.216) + (1.094 \pm 0.216) \times i_c^{-1/2}. \tag{7}$$
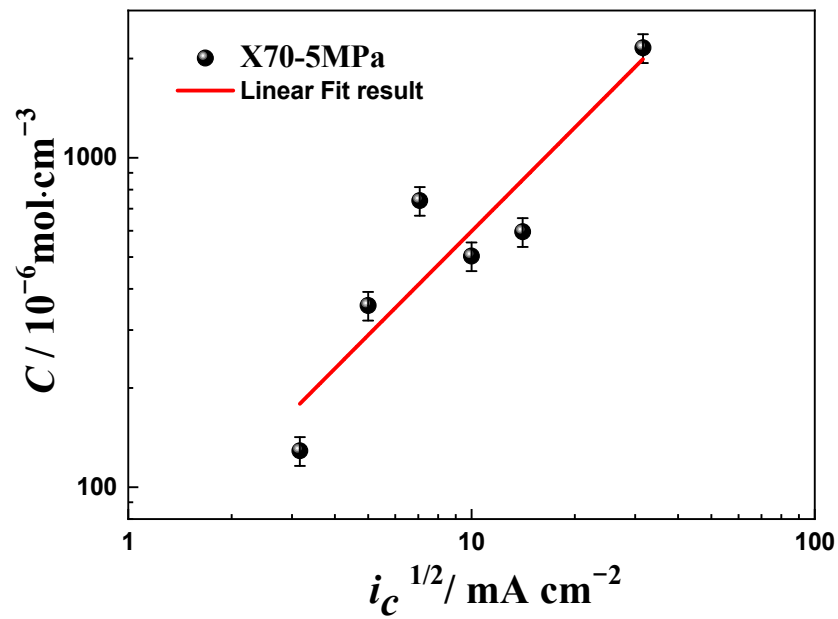
Figure 7. Variation of the hydrogen concentration with the charging current density of X70 steel after 24 h hydrogen charging under the 5 MPa hydrostatic pressure.
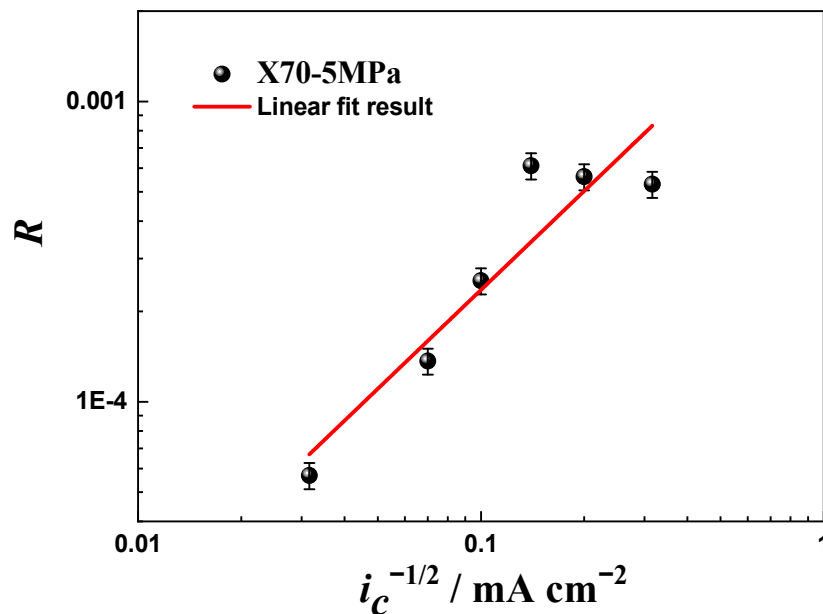
Figure 8. Variation of the hydrogen retention rate (R) with the hydrogen-charging current density after the 24 h hydrogen charging of X70 steel under the 5 MPa hydrostatic pressure.

Through the analyses above, we drew the conclusion that the average hydrogen concentration rose with the hydrogen-precharging current density. Meanwhile, the efficiency was reduced with the increases of the hydrogen-precharging current density.

3.3. Effect of the Hydrogen Charging on the SCC Susceptibility of X70 Steel under High Hydrostatic Pressure

3.3.1. SSRT Tests

Figure 9 shows the SSRT results of X70 steel under a simulated 500 m deep seawater environment with different current densities of 10, 25, 50, 100, 200, and 1000 mA/cm^2. The

elongation (δ), area reduction (ψ), and true strain (ε) of the SSRT experiments are listed in Table 1. The parameters were obtained through the following equations:

$$\delta = \Delta L/L \times 100\%, \tag{8}$$

$$\psi = \Delta A/A0 \times 100\%, \tag{9}$$

$$\varepsilon = \ln(1 + \Delta L/L), \tag{10}$$

where ΔL is the length variation after fracture, ΔA is the cross-sectional area after fracture, and L is the gauge length of the specimen.
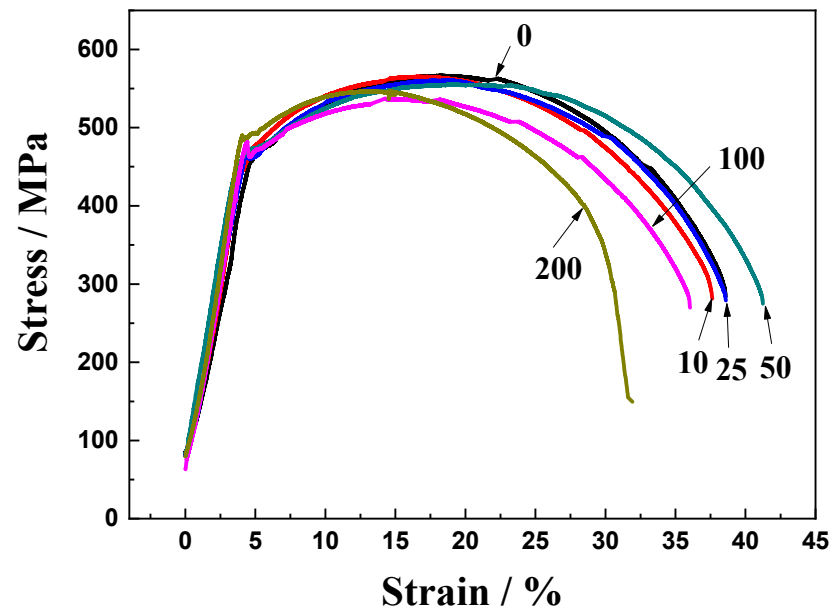
Figure 9. Stress–strain curves of 24 h hydrogen precharging with different current densities in the simulated 500 m deep seawater environment.

Table 1. The elongation rates (δ), area reductions (ψ), and true strains (ε) of the slow strain rate tensil (SSRT) after 24 h hydrogen charging with different current densities.

Parameter	Hydrogen-Charging Current Density (mA/cm^2)					
	0	10	25	50	100	200
δ (%)	36.7 ± 0.6	35.8 ± 0.3	36.9 ± 0.4	40.6 ± 0.5	33.3 ± 0.6	30.9 ± 0.9
ψ (%)	82.1 ± 0.2	82.5 ± 0.1	82.6 ± 0.2	81.8 ± 0.2	78.2 ± 0.5	72.7 ± 0.6
ε (%)	1.72 ± 0.01	1.74 ± 0.01	1.75 ± 0.01	1.70 ± 0.02	1.52 ± 0.04	1.30 ± 0.05

Comparing the series test results, we can see that hydrogen charging had a few effects on the yield strength (σ_s) but a distinct effect on the elongation of X70 steel under the 500 m seawater environment. No obvious change of δ can be observed for the hydrogen-precharging current density lower than 25 mA/cm^2. As the hydrogen-precharging current density reached 50 mA/cm^2, δ increased. However, when the current density continued to increase to higher than 100 mA/cm^2, δ decreased again.

From the result, we can see that the elongation rate (35.8%) at the 10 mA/cm^2 hydrogen-precharging current density was slightly reduced compared to that of the specimen without hydrogen precharging (36.7%). The elongation rate (35.9%) at the 25 mA/cm^2 hydrogen-precharging current density was similarly to that of the specimen without hydrogen precharging (36.7%). When the hydrogen-charging current density reached 50 mA/cm^2, the elongation rate rose to 40.6%. As the current density kept increasing to 100 mA/cm^2, the elongation rate was reduced as the current density increased. The variations of the area reduction (ψ) and the true strain (ε) with the hydrogen-charging

current density were in association with each other. When the hydrogen-precharging current density was lower than 25 mA/cm^2, both the area reduction (ψ) and the true strain (ε) had a slightly shift to the more positive side. When the hydrogen-precharging current density was higher than 50 mA/cm^2, both the area reduction (ψ) and the true strain (ε) had an obvious shift to the more negative side.

The elongation rate loss (I_δ), area reduction loss (I_ψ), and true strain loss (I_ε) were calculated to analyze the variation of the SCC susceptibility with the hydrogen-charging current density. Generally, the greater these indexes values are, the greater the SCC susceptibility is. Three SCC susceptibility parameters were calculated use Equations (11)–(13), respectively:

$$I_\delta = \left(1 - \frac{\delta_s}{\delta_0}\right) \times 100\%, \tag{11}$$

$$I_\psi = \left(1 - \frac{\psi_s}{\psi_0}\right) \times 100\%, \tag{12}$$

$$I_\varepsilon = \left(1 - \frac{\varepsilon_s}{\varepsilon_0}\right) \times 100\%, \tag{13}$$

where δ_s, ψ_s, and ε_s are the elongation rate, area reduction, and true strain after hydrogen charging, respectively; δ_0, ψ_0, and ε_0 are the elongation rate, area reduction, and true strain without hydrogen charging. The three SCC susceptibility parameters results are depicted in Figure 10.
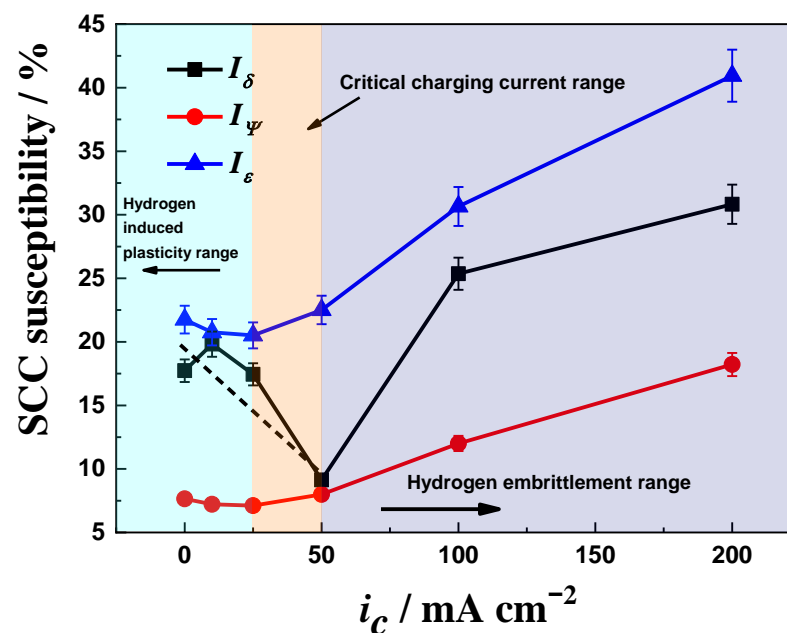
Figure 10. Variation of the stress corrosion cracking (SCC) susceptibility with the hydrogen-charging current density in the simulated 500 m deep seawater environment.

When the hydrogen-precharging current density was relatively lower than 25 mA/cm^2, slight decreases of I_ψ and I_ε were observed and a slight fluctuation of the I_δ was detected. When the hydrogen-precharging current densities were relatively higher than 25 mA/cm^2, all the three parameters exhibited an obvious shift to the more positive side, except a valley-like decrease of I_δ at 50 mA/cm^2 detected. As the analyses above, the SCC susceptibility of X70 steel decreased first and then increased with the hydrogen-charging current density. I_ψ and I_ε exhibited the lowest SCC susceptibility at the 25 mA/cm^2 hydrogen-precharging current density. The I_δ exhibited the lowest SCC susceptibility at the 50 mA/cm^2 hydrogen-precharging current density.

3.3.2. SEM Morphologies of the Fracture Surface

The SEM morphology of the fracture surface in each situation is shown in Figure 11. As shown in Figure 11(a1,a2), an obvious necking with a certain degree of a brittle fracture zone could be observed for the specimen without hydrogen charging. The necking increased gradually and the brittle fracture zone extended continuously, when the hydrogen-charging current densities were 10 and 25 mA/cm^2, as shown in Figure 11(b1,b2). With the current density increased, the necking shrunk gradually and the fracture surface tended to be smoother, as depicted in Figure 11(c1,f2), which represented a more noble brittleness characteristic of the X70 steel. Additionally, the fracture surfaces were more likely to display the quasi-cleavage morphologies. Tearing edges and dimples, as well as secondary cracks, can be detected almost in all fracture surfaces.
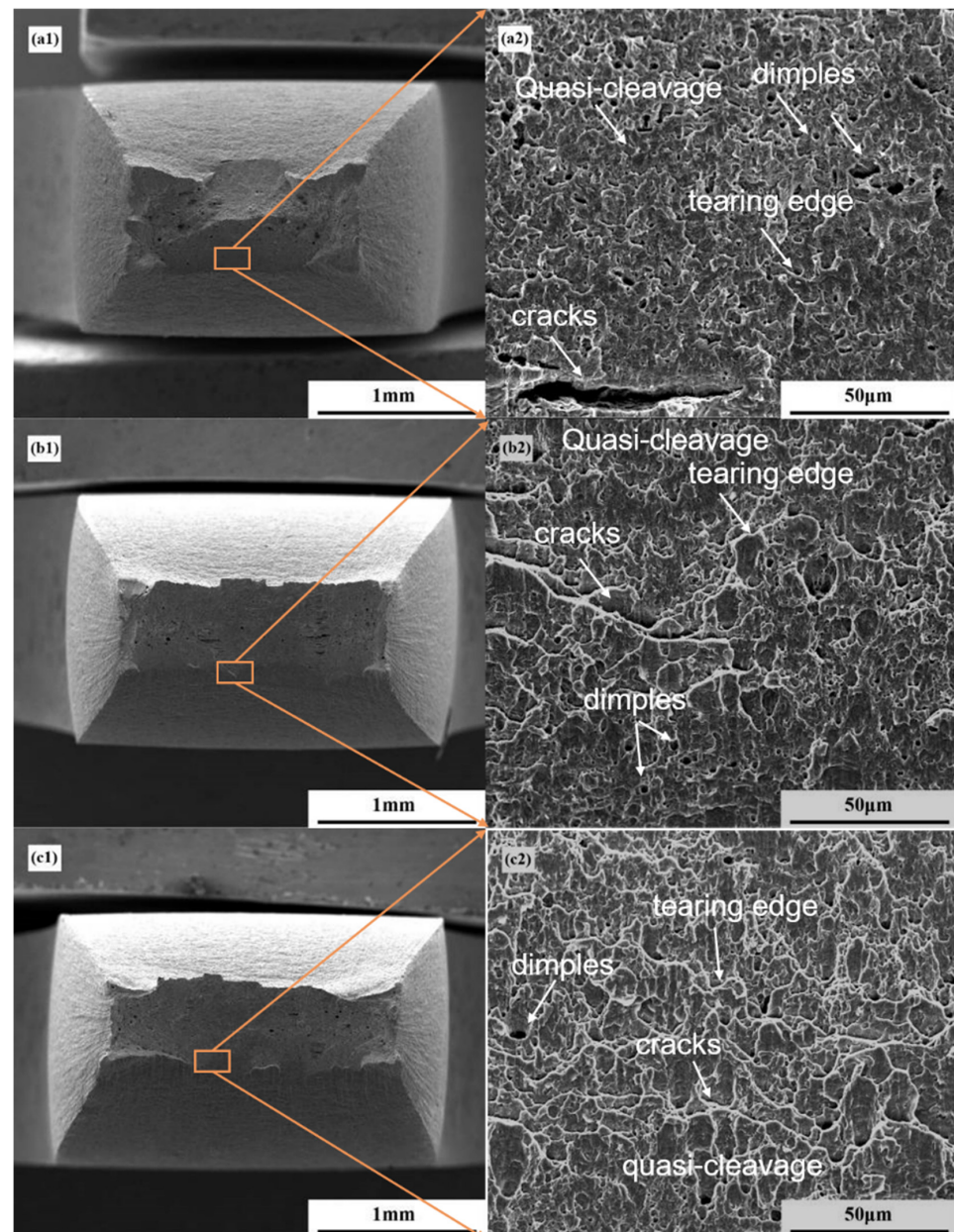
Figure 11. *Cont*.
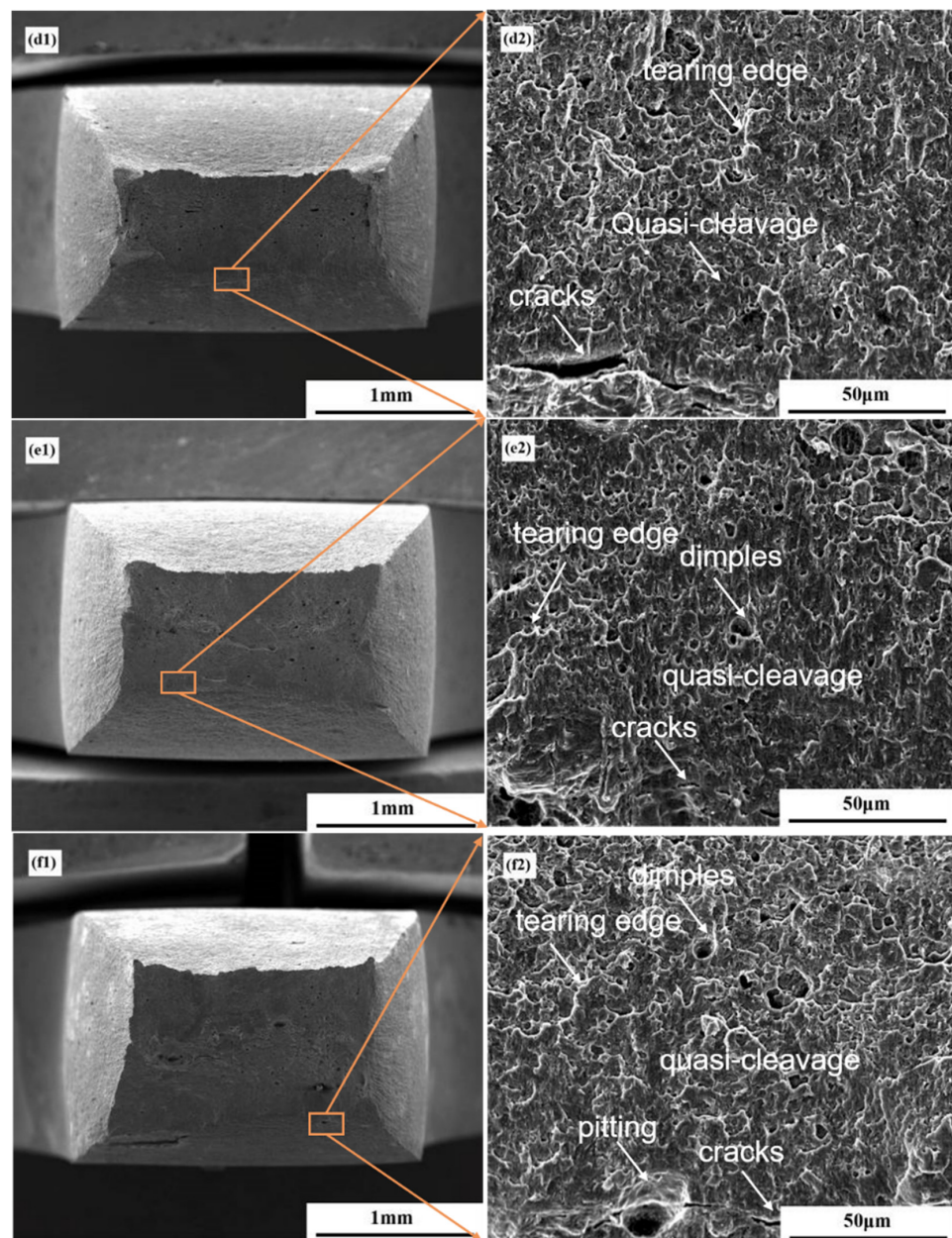
Figure 11. SEM morphologies of the fracture surface of the SSRT specimens at hydrogen-precharging current densities of 0 mA/cm^2 (**a1**,**a2**), 10 mA/cm^2 (**b1**,**b2**), 25 mA/cm^2 (**c1**,**c2**), 50 mA/cm^2 (**d1**,**d2**), 100 mA/cm^2 (**e1**,**e2**), and 200 mA/cm^2 (**f1**,**f2**).

The SEM morphologies of the adjacent side face of the fracture in each situation are shown in Figure 12. Microcracks can be found in the side faces of all the specimens. The crack development orientation was not intergranular, like zigzag but approximately a straight line, which indicated the transgranular development mode of all these cracks. Thus, the SCC development mode of X70 steel with hydrogen precharging in the simulated seawater environment was mostly transgranular stress corrosion cracking (TGSCC).

Some microcracks across the whole corrosion pits were detected during the process of observing the side face cracks, which are shown in Figure 13. These cross-microcracks revealed that the cracks were initiated at the corrosion pits in priority and then extended. Furthermore, more cracks in sizes and amounts in the zone concentrated with more corrosion pits. This illustrated that hydrogen promoted the anodic dissolution of X70 steel in the

simulated seawater environment. Meanwhile, the synergistic effects of the hydrogen and anodic dissolution led to the SCC.
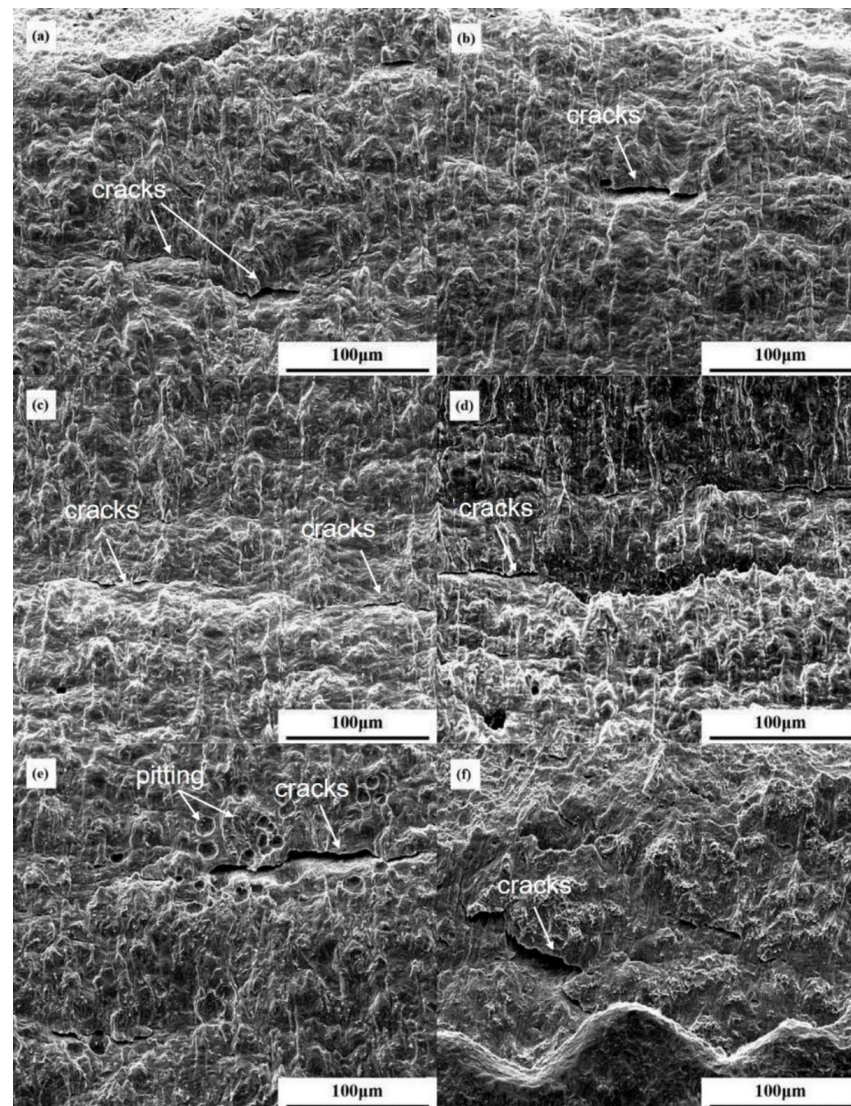
Figure 12. SEM morphologies of the side face of the SSRT specimens at hydrogen-precharging current densities of 0 mA/cm^2 (**a**), 10 mA/cm^2 (**b**), 25 mA/cm^2 (**c**), 50 mA/cm^2 (**d**), 100 mA/cm^2 (**e**), and 200 mA/cm^2 (**f**).
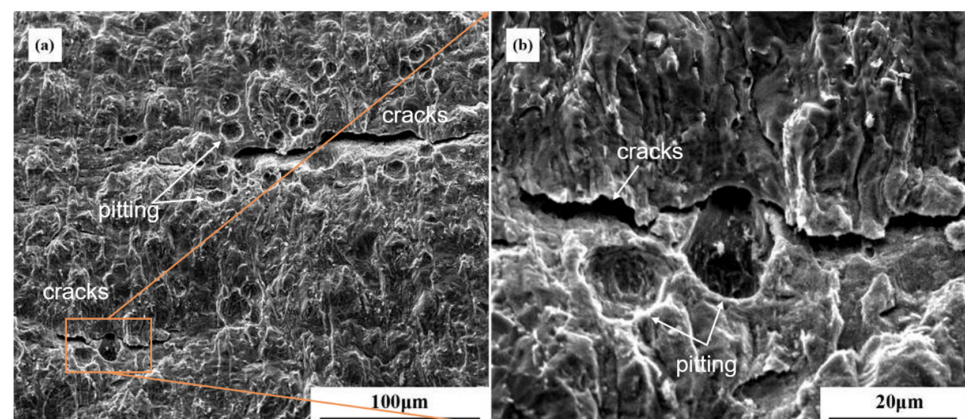
Figure 13. SEM morphologies (**a**) and the partial enlargement (**b**) of the side face of the SSRT specimens at the 200 mA/cm^2 hydrogen-precharging current density.

4. Discussion

Wang et al. [27] researched the effect of hydrogen on the fracture toughness K_{IQ} of X70 steel using the electrochemical hydrogen precharging method. Their result shows that when the hydrogen-precharging current density was relatively lower than 25 mA/cm^2, hydrogen promoted K_{IQ} for a slightly increase. They defined this current density as the critical hydrogen-charging current density. When the current density was relatively lower than this value, the hardening effect could increase the K_{IQ} by 11.8% at maximum. However, when the current density was relatively higher than this value, K_{IQ} decreased, as the hydrogen charging current density increased. As high as the current density increased up to 1000 mA/cm^2, K_{IQ} decreased by 13.7%. This kind of effect was also observed in pure iron [28]. Other researches [29,30] also represented that decreasing of the fracture toughness K_{IQ} of X series steel (X60, X70, X80, and X100) needs a sufficiently high hydrogen-precharging current density or a sufficiently long hydrogen-precharging time. Therefore, the hydrogen embrittlement of pipeline steel needs a sufficiently high hydrogen density. It is in association with our experiment result that the variation of the SCC susceptibility decreased first and then increased with the rising of the hydrogen-charging current density, which means the non-linearity relationship of the hydrogen effect on the SCC susceptibility. There exists a critical hydrogen current density that corresponds with the inflection point of the SCC susceptibility. This can be interpreted by using the hydrogen-induced local plastic model [31,32]. The diffused hydrogen in the metal may concentrate in the dislocation or elastic stress field and form into a Cottrell air mass. The distribution of the Cottrell air mass departs the dislocation and the elastic stress field and reduces their synergistic effect simultaneously. Therefore, the slip resistance of dislocation can be reduced, and the dislocation density can be promoted. As the hydrogen concentration is high enough, the main dislocation would accumulate and integrate at the dislocation source. As a result, the local shear stress is produced, and it increases the SCC susceptibility by promoting the initiation and growth of the crack. The fundamental principle behind the hydrogen embrittlement mechanism is that the presence of hydrogen in the lattice reduces the bond strength, and this leads to rupture at lower levels of stress [33,34].

The fracture morphologies depicted the brittle fracture zone was continuously extended as the hydrogen-charging current density increased. All the fractures depicted quasi-cleavage caused by the intensification of hydrogen embrittlement and the inhibition of anodic dissolution. It could be attributed to the residual hydrogen atoms concentrated in the traps or grain boundaries. As the hydrogen content reached the threshold value, it could lead to hydrogen embrittlement by the hydrogen-induced hardening impact [35,36]. According to the result of SSRT shown in Figure 8, the critical hydrogen-charging current densities I_ψ and I_δ of the SCC susceptibility can be obtained as 25 and 50 mA/cm^2, respectively. Generally, the value of 25 mA/cm^2 should be taken as the hydrogen-precharging current density for the SCC susceptibility reflected by I_ψ was always better than for I_δ. However, whether the value was actually the minimum of the SCC susceptibility is unclear. To obtain the minimum and more precise result, more experimental samples and more accurate measurements are needed. Therefore, the critical charging current value should be in the range of 25–50 mA/cm^2 in our tests. Additionally, the critical value means a competition mechanism between hydrogen-induced plasticity and hydrogen embrittlement [37–39]. It is often considered that hydrogen traps are expected to mitigate hydrogen embrittlement by reducing the local hydrogen concentration at crack initiation sites [40,41]. Therefore, for a relatively low concentration of hydrogen atoms, the trap sites play the main role in controlling the elongation and area reduction loss of the X70 steels.

5. Conclusions

In this study, the effect of the hydrogen permeation on the SCC behavior of X70 steel was studied by electrochemical tests, SSRT tests, as well as morphology characterizations. A possible mechanism about the effect of hydrogen on the SCC behavior of X70 steels was proposed. The main conclusions are as follows:

(1) The concentrations of the adsorbed hydrogen in X70 steel after hydrogen precharging under different hydrostatic pressures increased gradually and tended to be steady with the charging time. A high hydrostatic pressure promoted the hydrogen permeation of X70 pipeline steel by promoting the permeating rate and quantity.

(2) The adsorbed hydrogen concentration increased with the increase of the hydrogen-precharging current density, satisfying the relationship of $C \propto (1.047 \pm 0.223) \times i_c^{1/2}$. The hydrogen retention rate was reduced with the increase of the hydrogen-precharging current density, satisfying the relationship of $R \propto (1.094 \pm 0.216) \times i_c^{-1/2}$.

(3) The SCC susceptibility of X70 steel decreased first and then increased with the hydrogen-charging current density. The area reduction loss (I_ψ) and the true strain loss (I_ε) exhibited the lowest SCC susceptibility at the 25 mA/cm^2 hydrogen-precharging current density. The elongation rate loss (I_δ) exhibited the lowest SCC susceptibility at the 50 mA/cm^2 hydrogen-precharging current density. The critical charging current value should be in the range of 25–50 mA/cm^2.

Author Contributions: Conceptualization, X.L.; methodology, X.Y., Z.L. and F.S.; investigation, X.Y.; resources, C.D.; data curation, Q.L.; writing—original draft preparation, X.Y.; writing—review and editing, X.Y.; visualization, R.Z.; supervision, X.L. All authors have read and agreed to the published version of the manuscript.

Data Availability Statement: The raw/processed data required to reproduce these findings cannot be shared at this time, as the data are related to an ongoing study.

Conflicts of Interest: The authors declare no conflict of interest.

Abbreviations

SCC	stress corrosion cracking
SSRT	slow strain rate tensile
CP	cathodic protection
AD	anodic dissolution
HE	hydrogen embrittlement
HELP	hydrogen-enhanced localization plasticity model
HEDP	hydrogen-enhanced decohesion
SCE	saturated calomel electrode
TGSCC	transgranular stress corrosion cracking
I_C (mA/cm^2)	hydrogen-charging current density.
i_H (mA/cm^2)	hydroxide current density
C (10^{-6} mol/cm^3)	hydrogen concentration
Q (C)	electric charge quantity
R (%)	hydrogen retention ratio
t_0 (s)	Hydrogen-precharging time
σ_s (MPa)	yield strength
δ (%)	elongation rate
ψ (%)	area reduction
ε (%)	true strain
I_δ (%)	elongation rate loss
I_ψ (%)	area reduction loss
I_ε (%)	true strain loss
K_{IQ} (MPa·m$^{1/2}$)	fracture toughness
ΔL (m)	length variation after fracture
ΔA (m^2)	cross-sectional area after fracture
L (m)	gauge length
A (m^2)	original sectional area

References

1. Komai, S. Failure analysis and prevention in SCC and corrosion fatigue cases. *Int. J. Fatigue* **1998**, *20*, 145–154. [CrossRef]
2. Meresht, E.S.; Farahani, T.S.; Eshati, J. Failure analysis of stress corrosion cracking occurred in a gas transmission steel pipeline. *Eng. Fail. Anal.* **2011**, *18*, 963–970. [CrossRef]
3. Roccisano, A.; Luzin, V.M.; Lavigne, O.; Gamboa, E.; Griggs, J. High-pH inclined stress corrosion cracking in Australian and Canadian gas pipeline X65 steels. *Mater. Sci. Technol.* **2016**, *32*, 684–690.
4. Jidong, W.; Xueqing, H.; Wenlong, Q.; Chunyan, Z.; Yang, Z.; Yong, D.; Tao, Z.; Fuhui, W. Corrosion failure analysis of the 45-degree elbow in a natural gas gathering pipeline by experimental and numerical simulation. *Eng. Fail. Anal.* **2020**, *118*, 104889.
5. Wu, G.Y.; Zhao, W.W.; Wang, Y.R.; Tang, Y.F.; Xie, M. Analysis on corrosion-induced failure of shale gas gathering pipelines in the southern Sichuan Basin of China. *Eng. Fail. Anal.* **2021**, *130*, 105796. [CrossRef]
6. Liu, Z.Y.; Wang, X.Z.; Liu, R.K.; Du, C.W.; Li, X.G. Electrochemical and sulfide stress corrosion cracking behaviors of tubing steels in a H2S/CO2 annular environment. *J. Mater. Eng. Perform.* **2014**, *23*, 1279–1287. [CrossRef]
7. Akhi, A.H.; Dhar, A.S. Stress intensity factors for external corrosions and cracking of buried cast iron pipes. *Eng. Fract. Mech.* **2021**, *250*, 107778. [CrossRef]
8. Wan, H.; Song, D.; Cai, Y.; Du, C. The AC corrosion and SCC mechanism of X80 pipeline steel in near-neutral pH solution. *Eng. Fail. Anal.* **2020**, *118*, 104904. [CrossRef]
9. Song, L.; Liu, Z.; Li, X.; Du, C.; Guo, X.; Zhang, Y.; Wu, W. Influence of microstructure on stress corrosion cracking of X100 pipeline steel in carbonate/bicarbonate solution. *J. Mater. Res. Technol.* **2022**, *17*, 150–165.
10. Wang, S.; Lamborn, L.; Chen, W. Near-neutral pH corrosion and stress corrosion crack initiation of a mill-scaled pipeline steel under the combined effect of oxygen and paint primer. *Corros. Sci.* **2021**, *187*, 109511. [CrossRef]
11. Cui, Z.; Liu, Z.; Wang, L.; Li, X.; Du, C.; Wang, X. Effect of plastic deformation on the electrochemical and stress corrosion cracking behavior of X70 steel in near-neutral pH environment. *Mater. Sci. Eng. A* **2016**, *677*, 259–273. [CrossRef]
12. Niazi, H.; Eadie, R.; Chen, W.; Zhang, H. High pH stress corrosion cracking initiation and crack evolution in buried steel pipelines: A review. *Eng. Fail. Anal.* **2021**, *120*, 105013. [CrossRef]
13. Yang, X.; Yang, Y.; Sun, M.; Jia, J.; Cheng, X.; Pei, Z.; Li, Q.; Xu, D.; Xiao, K.; Li, X. A new understanding of the effect of Cr on the corrosion resistance evolution of weathering steel based on big data technology. *J. Mater. Sci. Technol.* **2022**, *104*, 67–80. [CrossRef]
14. Kang, Y.; Chen, W.; Kania, R.; Van Boven, G.; Worthingham, R. Simulation of crack growth during hydrostatic testing of pipeline steel in near-neutral pH environment. *Corros. Sci.* **2011**, *53*, 968–975. [CrossRef]
15. Yang, X.; Shao, J.; Liu, Z.; Zhang, D.; Cui, L.; Du, C.; Li, X. Stress-assisted microbiologically influenced corrosion mechanism of 2205 duplex stainless steel caused by sulfate-reducing bacteria. *Corros. Sci.* **2020**, *173*, 108746. [CrossRef]
16. Nguyen, T.-T.; Bolivar, J.; Shi, Y.; Réthoré, J.; King, A.; Fregonese, M.; Adrien, J.; Buffiere, J.-Y.; Baietto, M.-C. A phase field method for modeling anodic dissolution induced stress corrosion crack propagation. *Corros. Sci.* **2018**, *132*, 146–160. [CrossRef]
17. Ma, H.; Liu, Z.; Du, C.; Wang, H.; Li, C.; Li, X. Effect of cathodic potentials on the SCC behavior of E690 steel in simulated seawater. *Mater. Sci. Eng. A* **2015**, *642*, 22–31. [CrossRef]
18. Liu, Y.; Wang, J.W.; Liu, L.; Li, Y.; Wang, F.H. Study of the failure mechanism of an epoxy coating system under high hydrostatic pressure. *Corros. Sci.* **2013**, *74*, 59–70. [CrossRef]
19. Ge, Y.; Aaltio, I.; Hannula, S.-P. A Study of Hydrogen Charging of 10M Ni-Mn-Ga Single Crystal. *Mater. Today Proc.* **2015**, *2*, S859–S862. [CrossRef]
20. Yang, Z.; Kan, B.; Li, J.; Su, Y.; Qiao, L. Hydrostatic pressure effects on stress corrosion cracking of X70 pipeline steel in a simulated deep-sea environment. *Int. J. Hydrogen Energy* **2017**, *42*, 27446–27457. [CrossRef]
21. Sun, F.; Ren, S.; Li, Z.; Liu, Z.; Li, X.; Du, C. Comparative study on the stress corrosion cracking of X70 pipeline steel in simulated shallow and deep sea environments. *Mater. Sci. Eng. A* **2017**, *685*, 145–153. [CrossRef]
22. Westlake, D.; Satterthwaite, C.; Weaver, J. Hydrogen in metals. *Phys. Today* **1978**, *31*, 32–39. [CrossRef]
23. Abraham, D.P.; Altstetter, C.J. The effect of hydrogen on the yield and flow stress of an austenitic stainless steel. *Metall. Mater. Trans. A* **1995**, *26*, 2849–2858. [CrossRef]
24. Liang, Y.; Sofronis, P. Toward a phenomenological description of hydrogen-induced decohesion at particle/matrix interfaces. *J. Mech. Phys. Solids* **2003**, *51*, 1509–1531. [CrossRef]
25. Ramirez, M.F.; Hernández, J.W.; Ladino, D.H.; Masoumi, M.; Goldenstein, H. Effects of different cooling rates on the microstructure, crystallographic features, and hydrogen induced cracking of API X80 pipeline stee. *J. Mater. Res. Technol.* **2021**, *14*, 1848–1861. [CrossRef]
26. Yan, M.; Weng, Y. Study on hydrogen absorption of pipeline steel under cathodic charging. *Corros. Sci.* **2006**, *48*, 432–444. [CrossRef]
27. Hardie, D.; Charles, E.A.; Lopez, A.H. Hydrogen embrittlement of high strength pipeline steels. *Corros. Sci.* **2006**, *48*, 4378–4385. [CrossRef]
28. Chen, L.; Liu, M.Z.; Su, H.H.; Yin, W.Q.; Li, C.P. A study of hydrogen effect on deformation and fracture microprocess in pure iron. *Acta Metal. Sin.* **1981**, *17*, 541–548.
29. Han, Y.; Wang, R.; Wang, H.; Xu, L.Y. Hydrogen embrittlement sensitivity of X100 pipeline steel under different pre-strain. *Int. J. Hydrogen Energy.* **2019**, *44*, 22380–22393. [CrossRef]

30. Zhao, Y.; Wang, R. An investigation on mechanical behaviors of pipeline steel X70 after electrochemical hydrogen charging. *J. Chin. Soc. Corrosi. Prot.* **2004**, *24*, 293–296.

31. Ogawa, Y.; Iwata, K.; Okazaki, S.; Nakamura, M.; Matsubara, K.; Takakuwa, O.; Matsunaga, H. Fatigue crack-growth retardation after overloading in gaseous hydrogen: Revisiting the effect of hydrogen on crack-tip plastic-zone development. *Mater. Lett.* **2021**, *308*, 131115. [CrossRef]

32. Xing, X.; Zhang, Y.; Wang, S.; Li, Z.; Yang, C.; Cui, G.; Zhang, S.; Liu, J.; Gou, J.; Yu, H. Atomistic simulation of hydrogen-induced plastic zone compression during cyclic loading. *Int. J. Hydrogen Energy* **2020**, *45*, 15697–15709. [CrossRef]

33. Robertson, I.M.; Sofronis, P.; Nagao, A.; Martin, M.L.; Wang, S.; Gross, D.W.; Nygren, K.E. Hydrogen embrittlement understood. *Metall. Mater. Trans. A* **2015**, *46*, 2323–2341. [CrossRef]

34. Zhang, S.; Fan, E.; Wan, J.; Liu, J.; Huang, Y.; Li, X. Effect of Nb on the hydrogen-induced cracking of high-strength low-alloy steel. *Corros. Sci.* **2018**, *139*, 83–96. [CrossRef]

35. Dayal, R.K.; Parvathavarthini, N. Hydrogen embrittlement in power plant steels. *Sadhana* **2003**, *28*, 431–451. [CrossRef]

36. Song, L.; Liu, Z.; Li, X.; Du, C. Characteristics of hydrogen embrittlement in high-pH stress corrosion cracking of X100 pipeline steel in carbonate/ bicarbonate solution. *Constr. Build. Mater.* **2020**, *263*, 120124. [CrossRef]

37. Akiyama, E.; Akiyama, E.; Wang, M.; Wang, M.; Li, S.; Li, S.; Zhang, Z.; Zhang, Z.; Kimura, Y.; Kimura, Y.; et al. Studies of Evaluation of Hydrogen Embrittlement Property of High-Strength Steels with Consideration 431 of the Effect of Atmospheric Corrosion. *Metall. Mater. Trans. A* **2013**, *44*, 1290–1300. [CrossRef]

38. Oriani, R.A.; Josephic, P.H. Testing of the decohesion theory of hydrogen-induced crack propagation. *Scripta Metall.* **1972**, *6*, 681–688. [CrossRef]

39. Yang, X.; Du, C.; Wan, H.; Liu, Z.; Li, X. Influence of sulfides on the passivation behavior of titanium alloy TA2 in simulated seawater environments. *Appl. Surf. Sci.* **2018**, *458*, 198–209. [CrossRef]

40. Li, Q.; Xia, X.; Pei, Z.; Cheng, X.; Zhang, D.; Xiao, K.; Wu, J.; Li, X. Long-term corrosion monitoring of carbon steels and environmental correlation analysis via the random forest method. *NPJ Mater. Degrad.* **2022**, *6*, 1. [CrossRef]

41. Yang, X.; Liu, M.; Liu, Z.; Du, C.; Li, X. Failure analysis of a 304 stainless steel heat exchanger in liquid sulfur recovery units. *Eng. Fail. Anal.* **2020**, *116*, 104729. [CrossRef]